

## Article

# Assessment of Molecular Additives on the Lifetime of Carbon-Based Mesoporous Perovskite Solar Cells

Rodolfo López-Vicente <sup>1,\*</sup>, José Abad <sup>2</sup>, Javier Padilla <sup>2</sup> and Antonio Urbina <sup>1,\*</sup><sup>1</sup> Department of Electronics, Technical University of Cartagena, Pz Hospital 1, 30202 Cartagena, Spain<sup>2</sup> Department of Applied Physics, Technical University of Cartagena, Pz Hospital 1, 30202 Cartagena, Spain; jose.abad@upct.es (J.A.); javier.padilla@upct.es (J.P.)

\* Correspondence: rodolfo.lopez@upct.es (R.L.-V.); antonio.urbina@upct.es (A.U.)

**Abstract:** Perovskite solar cells have progressed very steadily, reaching power conversion efficiencies (PCE) beyond 20% while also improving their lifetimes up to 10,000 h. A large number of cell architecture and materials for active, transporting and electrode layers have been used, either in blends or in nanostructured layers. In this article, a set of perovskite solar cells have been designed, fabricated and characterized with special focus on their lifetime extension. The inclusion of 5-aminovaleric acid iodide (5-AVAI) as interlayer in a methyl-amino lead-iodide (MAPI) perovskite solar cell has provided additional stability in cells with PCE > 10% and  $T_{80} = 550$  h. Experiments for up to 1000 h with solar cells at maximum power point under continuous illumination with solar simulator have been carried out (1 kW/m<sup>2</sup>, AM1.5G, equivalent to more than six months of outdoor illumination in locations such as Southeast Spain, with an average irradiation of 1900 kWh/m<sup>2</sup>/year). The addition of molecular additives in the bulk active layer and ETL and carbon layers not only allows better carrier transport, but also increases the stability of the perovskite solar cell by reducing ion migration within the bulk MAPI and between the different layers. Engineered interfaces with ZrO<sub>2</sub> between the TiO<sub>2</sub> and carbon layers contribute to reducing degradation.

**Keywords:** hybrid solar cells; perovskite solar cells; photovoltaic emerging technologies; lifetime and degradation



**Citation:** López-Vicente, R.; Abad, J.; Padilla, J.; Urbina, A. Assessment of Molecular Additives on the Lifetime of Carbon-Based Mesoporous Perovskite Solar Cells. *Energies* **2021**, *14*, 1947. <https://doi.org/10.3390/en14071947>

Academic Editor: Jaemin Kong

Received: 22 February 2021

Accepted: 26 March 2021

Published: 1 April 2021

**Publisher's Note:** MDPI stays neutral with regard to jurisdictional claims in published maps and institutional affiliations.



**Copyright:** © 2021 by the authors. Licensee MDPI, Basel, Switzerland. This article is an open access article distributed under the terms and conditions of the Creative Commons Attribution (CC BY) license (<https://creativecommons.org/licenses/by/4.0/>).

## 1. Introduction

Perovskite solar cells in tandem architecture combined monolithically with a crystalline silicon cell are approaching the 30% power conversion efficiency (PCE) milestone: Oxford PV has recently announced a 29.5% in a 1 cm<sup>2</sup> laboratory solar cell as certified by the USA National Renewable Laboratory, thus consolidating again the lead of Prof. Henry Snaith's group in Oxford [1,2]. When only perovskite active layer material is included in the tandems, they achieve the 20% milestone by benefiting from the possibility of using benchmark methyl ammonium lead iodide active layer with other wide band gap combinations of absorbers [3]. Nevertheless, most long-term stable perovskite solar cells present PCE in the range from 10% to 15%, although different methods to report lifetimes make a straightforward comparison of reported results difficult. In this regard, some efforts are being carried out in order to apply the well-known ISOS protocols already used in organic solar cells to perovskite solar cells [4,5]. The hysteresis which is observed in the current-voltage characteristics of most perovskite solar cells generates further discrepancy when reporting results, so new figures of merit and common procedures to quantify hysteresis have been recommended [6]. Therefore, research in perovskite solar cells has been oriented not only to reach better efficiencies but also, especially in the past few years, to extend their lifetime. At the same time, other additional concerns such as reducing toxic content of the material embedded in the cells (lead, spiro-OMeTad) or required in the processing steps (halogenated solvents) have been taken into consideration. The equilibrium required to

achieve high PCE, long lifetimes and reduced negative environmental impacts is guiding most research efforts in the field [7].

One of the research lines is the engineering of interfaces between the different layers of the solar cell, with special focus both on electron and hole transporting layers; this strategy has three aims: firstly, it tries to enhance carrier collection from active layer to electrodes by creating a ladder of available energy levels in valence and conduction bands (or HOMO/LUMO respectively); secondly, it tries to reduce ion migration, which is the main cause for hysteresis (although ion diffusion has also been reported in hysteresis-free solar cells [8]) and finally, it may contribute to reducing degradation, since the interfacial layer may block moisture or other contaminants' penetration from the atmosphere and avoid interlayer contamination. The most commonly used hole transporting layer (HTL) has been spiro-OmeTAD [9–13], followed by PCBM [14,15], conjugated polymers such as P3HT [16], PTAA [17,18] or PEDOT:PSS [19] and most recently transition metal oxides, like NiO, showing very good results in terms of extended lifetime [20,21]. HTL-free architectures have attracted attention, since on the one hand they avoid the toxic spiro-OmeTAD (toxic because of the chemicals required in its processing [22]), and on the other hand they avoid chemical contamination of the active layer: carbon scaffolds are the most successful approach to HTL-free options, considering carbon as the electrode itself (although it may be argued that it is an HTL layer when complemented by Ag or Au final metallization). The easier processing of the carbon ink and the possibility of infiltrating the active layer make this technological option one of the best for a cheap and reliable manufacturing process [23,24]. When considering the electron transporting layer (ETL), the most frequently used material is TiO<sub>2</sub>, with the inclusion of both compact and mesoporous layers, which is present in most of the previously cited references; another common option is the use of zinc oxide either in layers, nanoparticles or nanorod structures [16,25–27], aluminum oxide [28–31], molybdenum oxide [32–34] and zirconium oxide [25]. In the case of perovskite solar cells based on carbon “shells” to be infiltrated, the role of this additional metal oxide ETL layer is not only improving the electron transport but also preventing a short circuit between the carbon and the TiO<sub>2</sub> mesoporous material acting as electron transporting layer usually in contact with the transparent conducting oxide indium-doped or fluorine-doped tin oxide (ITO, FTO respectively).

Regarding the active layer, the benchmark methyl-ammonium lead iodide (MAPI) has been modified, usually with the objective of getting rid of the potentially toxic lead by total or partial substitution by tin [35,36]. Although the initial efforts led to lower PCE, recent results show efficiencies higher than 20% [37,38]; additionally, cesium substitution leads to good results [31]. However, the most recent approach to the main focus on extending the lifetime has been the addition of molecular dopants to the active layer. A broad range of molecules have been tested, and most results confirm the creation of monolayers on top of the crystalline grains of the active layer or in the interface between the active layer and the HTL or ETL layers [39,40]. The use of these additives has provided a jump in lifetimes from a common 500 to 1000 h range to 8600 h with the first attempts, and now well over 10,000 h [7].

The use of additives has been revealed as an efficient tool to prevent ion migration by means of the resulting improved crystallinity, grain size and surface coverage [41,42].

In this work, four different additives have been used: the well-known 5-aminovaleric acid iodide (5-AVAI) and three proposed alternatives: 4-aminobenzoic acid (PABA), terephthalic acid (TPA) and 3-phosphonopropionic acid (3-HPP). All of these additives have functional groups, such as the hydroxyl group (-OH), carboxyl group (-COOH) and nitrogen groups (-NH<sub>2</sub>) with different acidic character. As hydrogen bonds of these groups can interact with Pb<sup>2+</sup> or I<sup>-</sup> ions, therefore reducing ion migration, the expected effect of the inclusion of these additives is an extended lifetime and reduced hysteresis [43]. The 5-AVAI is an additive widely employed in triple mesoscopic solar cells [41,42]. Increasing efficiencies and stability as a result of the interaction of its amino and carboxylic groups with halide perovskites has been reported [44–46]. Terephthalic acid (TPA), a frequently

used chemical in the petrochemical industry, has previously been incorporated in the perovskite precursor solution, resulting in better moisture resistance and better device thermal and ambient stability [47,48]. The 4-aminobenzoic acid (PABA) is an amino acid that can block UV radiation and is commonly used in cosmetic products as a sunscreen. The PABA molecule has a carboxylic group and an amino group. It has been reported that PABA can enhance  $V_{oc}$ , FF and PCE in PSCs; this additive contributes to improving the morphology in the perovskite film and decreasing the carrier trap states, leading to an improvement of the performance of the devices [49,50]. Finally, 3-phosphonopropionic acid (H3PP) is a beta amino acid with an amino group and a phosphonic group. This small molecule was used in this work as an organic modifier due to the strong anchoring capability of the phosphonic group.

In this article, we present results which build upon a large amount of previous published work on molecular additives. We have used a carbon-based HTL-free architecture with the addition of a  $ZrO_2$  scaffold layer. The fabricated cells provide a range of good efficiencies (>10% in the best case) with large lifetimes for one of the additives that has been studied in more detail (5-amino valeric acid iodide, 5-AVAI). Then, other additives have been tested with the same architectures and optimized thickness of the layers and additive concentration, although with lower resulting PCE and lifetimes. In Section 2 materials and methods are described, followed by two sections in which results are presented and discussed. Conclusions are presented in Section 5.

## 2. Materials and Methods

Perovskite solar cells with methyl-ammonium lead iodide (MAPI) active layer and different molecular additives were fabricated and characterized. All the cells were fabricated by infiltration of a titania/zirconia/carbon shell with metal oxide electron transporting layers; they did not include any hole transporting layers (HTL-free cells). Electrodes were the same for all samples. A detailed description of cell fabrication is provided in Section 2.1, while the current-voltage (I–V) characterization and the degradation experiment, which was the same for all samples, is explained in Section 2.2.

### 2.1. Sample Fabrication

Hybrid perovskite solar cells were fabricated following a standard procedure [24,51]. The active layer was the benchmark methyl-ammonium lead iodide (MAPI) perovskite structure. An n-type  $TiO_2$  electron transporting layer was deposited on the transparent conducting substrate, leading to a n-i-p structure, and therefore the architecture of the cell was normal (also called regular or standard) [52]. Metal oxide electron transporting layers were screen-printed on top of a fluorine doped tin oxide (FTO), CVD coated glass substrate, with sheet resistance  $R_s \sim 8 \Omega/sq$  and total transmission around 80% in the 400–800 nm band (SOLEMS TEC 7/2.2). A first compact c- $TiO_2$  layer was deposited by spray pyrolysis from a 10% molar Titanium di-isopropoxide bis-acetylacetonate (Sigma Aldrich) solution in isopropyl alcohol dried and thermally annealed at 450 °C for 10 min in air. The following layers were deposited by screen printing. The pastes used for screen printing were  $TiO_2$  paste DSL 30NR-D (Dyesol),  $ZrO_2$  paste Zr-Nanoxide ZT/SP (Solaronix, particle size 20–40 nm, at 18% wt. in suspension with terpineol and other organic binders). These structures were covered by a screen-printed carbon-based layer (using carbon paste C2150317D3, Gwent Group), delivering a structure called the “shell”. Different threads were used in a commercial SA111576 Uniprint PM screen printer, with aperture of 40  $\mu m$  for the metal oxide pastes and 90  $\mu m$  for the carbon paste. The screen-printed layers were considered mesoporous after a thermal annealing process of 30 min at 450 °C. This shell was then infiltrated by spin-coating (the so-called “single step” method), with the perovskite solution prepared by using the usual precursors lead iodide  $PbI_2$  (purity 99%, TCI), MAI  $CH_3NH_3I$  (purity 98%, Dyesol) dissolved in  $\gamma$ -butyrolactone (GBL, purity 99%, Sigma Aldrich) and a final back hole collecting electrode was again screen-printed using conductive silver paste C2081126P2 (Gwent Group).

A schematic structure of the band gaps, conduction and valence band (for the semi-conducting materials) and work function for the carbon and metal electrodes are presented in Figure 1A. Ideally, the MAPI + additive active layer infiltrates the carbon and the mesoporous layers of  $ZrO_2$  and  $TiO_2$ . The  $ZrO_2$  layer prevents the electrical short-circuit between the  $TiO_2$  electron transporting layer and the carbon scaffold, which is acting as hole collecting layer (and connected to the Ag electrode). This reference structure was modified with the inclusion of different additives into the active layer: 5-aminovaleric acid iodide (5-AVAI), terephthalic acid (TPA), para-4-aminobenzoic acid (PABA) and 3-phosphono-propionic acid (H3PP) (molecular structures shown in Figure 1B). In all cases, additives were mixed at 3% molar concentration with the MAPI perovskite precursors before infiltration. The same solvent GBL was used in all cases, with the exception of TPA, where dimethyl formamide anhydrous (DMF, purity 99% Sigma Aldrich) was used. All molecular additives were included in the bulk of the active layer during the solution stage of MAPI preparation. Four kinds of samples were tested, as described in Table 1, the first group of three samples (A, B, C) all contained 5-AVAI but differed in the concentration of 5-AVAI added to the solution precursor of the MAPI active layer. The optimum weight concentration that delivered the best PCE results for the 5-AVAI additive (3% molar) was used as the optimal concentration for the other additives.

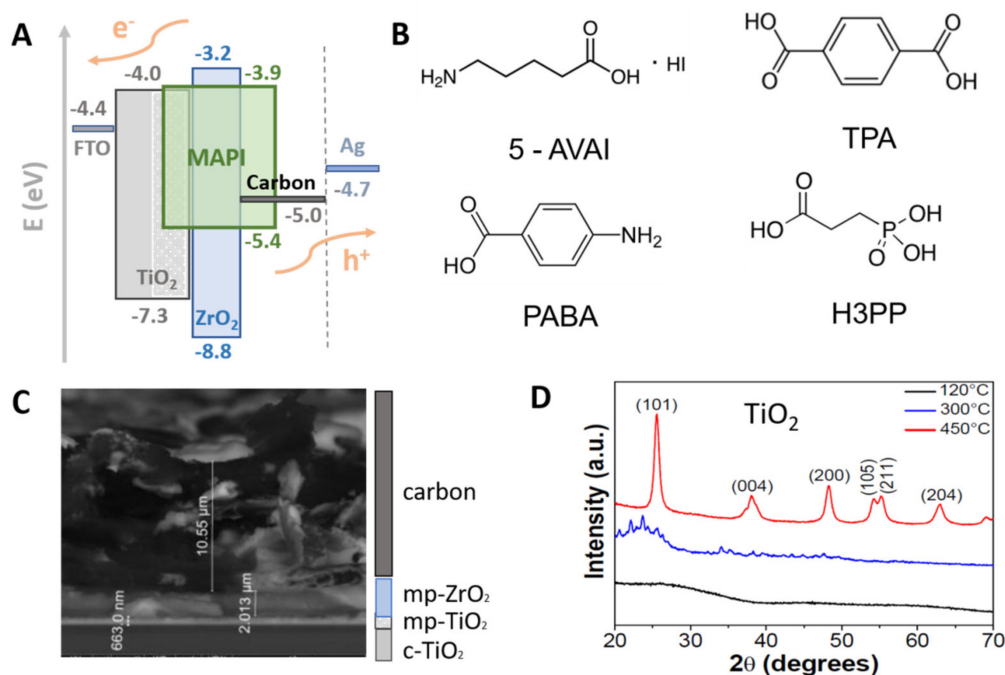


**Figure 1.** (A) Schematic structure of band gaps and work function of the different layers of the solar cells; (B) Molecular structure of the four additives used in the methyl-amino lead-iodide (MAPI) layer: 5-amino-valeric acid iodide (5-AVAI), terephthalic acid (TPA), para-4-aminobenzoic acid (PABA) and 3-phosphono-propionic acid (H3PP); (C) SEM image of the shell used to infiltrate the MAPI, showing the layers of compact and mesoporous  $TiO_2$ , mesoporous  $ZrO_2$  and carbon; (D) XRD of anatase  $TiO_2$  at different temperatures.

**Table 1.** Electrical parameters of the perovskite solar cells calculated as an average of 24 cells of each group (\* this cell presented reversed hysteresis when compared to the other cells). Scan column indicates forward (F) or backwards (reverse, B) sweep of voltage during the J–V measurement. HF<sub>1</sub> and HF<sub>2</sub> are the hysteresis factors, as defined in Section 2.2.

Cells	Additive	Scan	J <sub>sc</sub>	V <sub>oc</sub>	FF	PCE	HF <sub>1</sub>	HF <sub>2</sub>
			mA/cm <sup>2</sup>	V		%	mW/cm <sup>2</sup>	mW/cm <sup>2</sup>
A	5-AVAI (1%)	F	20.61 ± 1.57	0.73 ± 0.06	38.2 ± 6.5	5.69 ± 0.24	3.42	1.73
		B	23.56 ± 2.36	0.76 ± 0.06	59.4 ± 7.7	10.61 ± 1.40		
B	5-AVAI (5%)	F	12.89 ± 1.34	0.67 ± 0.07	27.3 ± 4.3	2.32 ± 0.82	6.68	4.33
		B	24.53 ± 3.41	0.70 ± 0.07	54.3 ± 6.2	9.28 ± 0.94		
C	5-AVAI (3%)	F	12.27 ± 1.67	0.60 ± 0.06	23.5 ± 4.8	1.70 ± 0.73	7.69	4.50
		B	25.84 ± 2.87	0.76 ± 0.06	56.8 ± 6.8	10.85 ± 1.69		
D	PABA	F	4.47 ± 0.40	0.70 ± 0.06	45.8 ± 6.8	1.43 ± 0.12	3.79	2.63
		B	9.70 ± 0.46	0.77 ± 0.07	69.4 ± 9.6	2.53 ± 0.65		
E	TPA	F	10.53 ± 2.44	0.70 ± 0.06	42.3 ± 5.3	3.30 ± 0.85	−2.97 *	−1.89 *
		B	8.01 ± 2.06	0.70 ± 0.07	45.9 ± 5.7	2.70 ± 0.85		
F	H3PP	F	2.83 ± 0.40	0.63 ± 0.06	51.0 ± 8.7	0.90 ± 0.10	1.16	0.81
		B	3.57 ± 0.42	0.70 ± 0.07	54.7 ± 9.2	1.37 ± 0.21		

## 2.2. Sample Characterization

The structure of the samples was characterized by a transversal scanning electron microscopy image, where the thickness of the different layers was measured (Figure 1C). The thickness of the layers constituting the infiltrated shell were 600 nm mp- TiO<sub>2</sub>; 2 μm mp- ZrO<sub>2</sub> and 10 μm carbon. An x-ray diffractogram of the TiO<sub>2</sub> layer was measured at different temperatures, showing that crystallinity was achieved after 450 °C thermal annealing; the diffractogram was fitted to reference code 00-004-0477 demonstrating a tetragonal anatase phase (I41/amd space group) as shown in Figure 1D.

Current-voltage (I–V) characteristics of the unencapsulated samples were measured by applying a voltage bias between the electrodes and sweeping the voltage between −1 V to +1 V (forward) and from +1 V to −1 V (backward) in order to measure the hysteresis appearing in most samples. The sweeping procedure was carried out always at the same voltage scan rate of 0.06 V/s. Voltage was applied with a programmable voltage source Keithley Mod. 230, and current was measured with an electrometer Keithley Mod. 6514. Since I–V curves were measured both forward and reverse at an initial stage, the hysteresis was obtained and quantified as the difference between the areas of integrated current from V = 0 to V = V<sub>oc</sub> for both traces. This method provided a “hysteresis factor” (HF<sub>1</sub>) defined as:

$$HF_1 = \int_0^{V_{oc}} (I_{backward}(V) - I_{forward}(V))dV \quad (1)$$

which provides a value slightly different when compared with the difference of delivered power at mpp between forward and backward bias, which can be defined as a second, single-point “hysteresis factor” (HF<sub>2</sub>) defined as:

$$HF_2 = P_{mpp,backward} - P_{mpp,forward} \quad (2)$$

Both HF<sub>1</sub> and HF<sub>2</sub> are included in Table 1 with other standard parameters.

For the long-term degradation experiments, I–V measurements were carried out for 1000 h (one every hour and only in backward bias between +1 V and −1 V), while the samples were kept polarized at maximum power point until a new I–V curve was measured (this is in line with ISOS-L1 and ISOS-V3 protocols [4]). This protocol was applied by using LabView-based software developed in our laboratory. The I–V characteristics were measured under ambient atmosphere (air), with stable laboratory temperature (25 °C) and relative humidity (40% ± 2%). The illumination was provided by an ABET AM1.5 Class AAA solar simulator, kept at constant irradiance of 1 kW/m<sup>2</sup> for 1000 h (a mask was used guaranteeing that active area of the cell was 7.1 mm<sup>2</sup>). This time under 1 Sun

irradiance is equivalent to several months under ambient conditions depending on the particular geographical location for an outdoor experiment, in particular for Southeast Spain with insolation values of more than 1900 kWh/m<sup>2</sup> per year in some locations, the degradation experiment can be considered to an equivalent outdoor illumination of more than six months. The experiment is not equivalent to a full outdoor experiment, since irradiance variations and temperature cycling (during day and night) as well as possible rain, wind, dust and other effects were not taken into consideration.

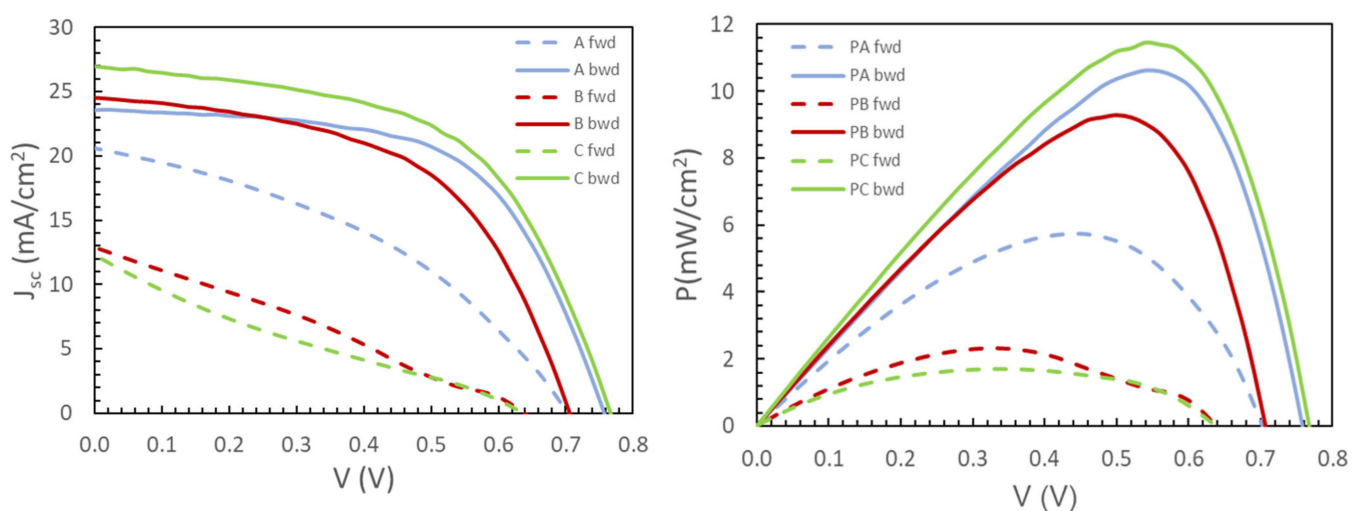
Electrical parameters (short circuit current ( $I_{sc}$ ), open circuit voltage ( $V_{oc}$ ) and power conversion efficiency (PCE)) of each of the one thousand I–V curves measured for each sample during each degradation experiment were obtained; additionally, maximum power point current and voltage ( $I_{mpp}$  and  $V_{mpp}$ ) and power delivered at mpp ( $P_{mpp}$ ) were also recorded for backward bias, which allowed us to calculate the filling factor (FF) for the backward branch of the I–V curve.

### 3. Results

The results section is organized in two subsections: the first one corresponds to initial sample characterization and hysteresis analysis for the six kinds of samples, of which 24 samples were prepared, thus providing some statistics. Best cell values are provided in the tables. The long-term degradation study is presented in Section 3.2 and was carried out in each case with the best cell of each kind that was identified by the initial experiment.

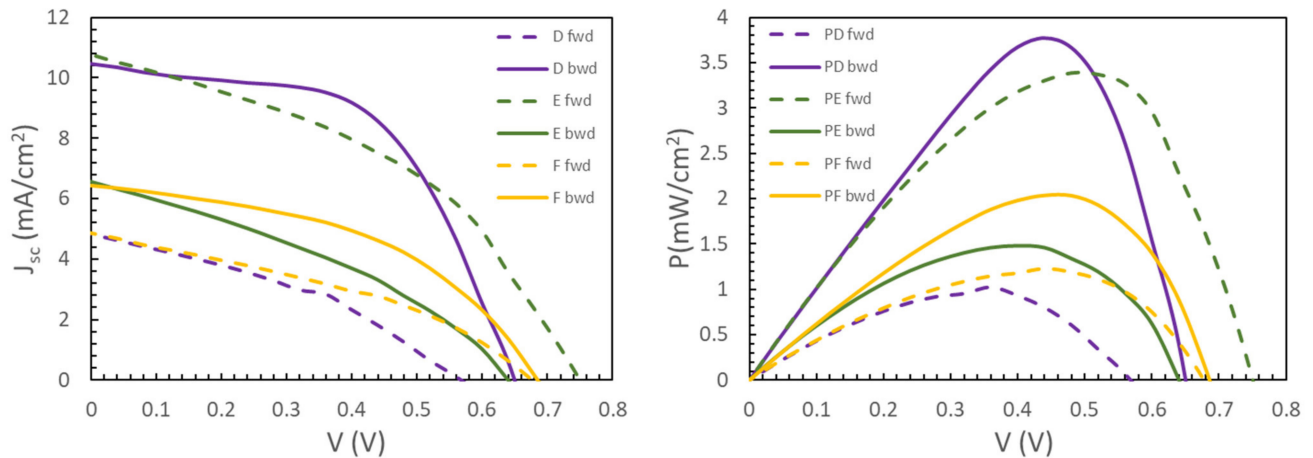
#### 3.1. Initial Characterization: I–V Curves and Hysteresis

Figure 2 shows the best cell results for the initial characterization by current density–voltage (J–V) and power density–voltage (P–V) curves of the MAPI samples with 5–AVAI additive at different weight concentration: 1% (A), 5% (B) and 3% (C). The grouping rationale was applied after the long-term experiment, since three samples delivered a much shorter lifetime than the others. The hysteresis shown by all samples was large, with the exception of one cell (A), although, as can be seen in Section 3.2, this did not translate into the longest lifetime, which was obtained by cell C, which had significant hysteresis.



**Figure 2.** Current density–voltage (J–V) (left) and power density–voltage (P–V) (right) curves of the best MAPI perovskite solar cell with 5–AVAI additives, with different weight concentrations: 1% (A), 5% (B) and 3% (C), all of them showing hysteresis between the forward (slashed line) and backward (continuous lines) sweep.

In Figure 3, the I–V and P–V curves for the PABA (D), TPA (E) and H3PP (F) additives are shown. In this case, the initial power efficiency was lower and hysteresis larger than in the previous 5–AVAI group. Furthermore, cell E (TPA) operated in a different way, since the larger power was delivered in forward sweep (as illustrated by the minus sign in the calculated hysteresis factors shown in Table 1).



**Figure 3.** Current-voltage (I–V) (left) and power-voltage (P–V) (right) curves of the best MAPI perovskite solar cell with 4-aminobenzoic acid (PABA) (D), terephthalic acid (TPA) (E) and 3-phosphonopropionic acid (H3PP) (F) additives, all of them showing hysteresis between the forward (slashed line) and backward (continuous lines) sweep. All backward sweeps showed better performance, except the E cell, which was better in forward sweep.

The average electrical parameters of the six groups of samples (24 samples per group) are included in Table 1, which is presented to emphasize the rationale guiding the sample preparation strategy: once the “shell” was optimized (thickness of respective layers as described above), the concentration of 5-AVAI, the first additive used, was explored, starting with a low concentration (1%, cell A), then 5% (cell B), then higher concentrations which all delivered failed cells, and back to 3% (cell C), which delivered the best PCE and longer lifetimes. Based on this, the same concentration was applied to the other additives in order to compare all of them at the same weight concentration (3%, cells D, E and F).

### 3.2. Long Term Degradation Experiments

All samples suffered degradation during the long-term experiment, with three of the samples showing rapid degradation after 100 h (D, E, F) while the other three (A, B, C) showed much longer lifetimes. Loss in photocurrent and PCE in this case was only appreciated when the experiment was carried out up to 1000 h. In A–F samples, the I–V curves were recorded by sweeping the voltage backwards (or reverse), that is, from 1 V to –1 V with a scan rate of 0.06 V/s. For sample E, the voltage was applied forwards (from –1 V to 1 V) at the same scan rate. One full I–V curve was recorded every hour during the 1000 h experiment; between two sweeps, the samples were kept under illumination at maximum power point (operating conditions). Figure 4 shows the evolution of short circuit current ( $J_{sc}$ ) and PCE. The logarithmic scale in the current axis emphasizes the evolution and also demonstrates that a nonexponential trend was followed.

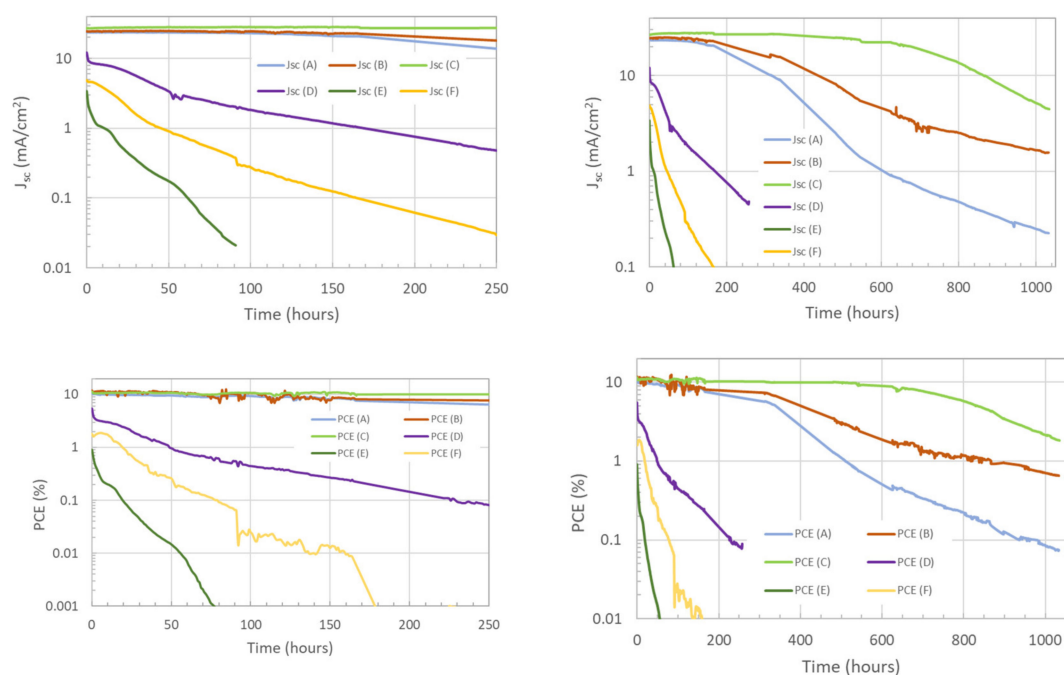


**Figure 4.** Short circuit current ( $J_{sc}$ , upper plots) and power conversion efficiency (PCE, lower plots) of the six samples. Logarithmic axis for short circuit current emphasizes the rapid drop for the set of D, E, F samples (up to 250 h) while the A, B, C had much longer lifetimes, extended more than 1000 h. For better visualization, left figures show the first 250 h of the experiments while right figures show the complete experiments.

#### 4. Discussion

In order to quantify the lifetime of the cells and to compare the different additives with other published data, standard parameters were used. From the PCE time evolutions shown in Figure 4,  $T_{80}$ ,  $T_{50}$  and  $T_{20}$  could be extracted (shown in Table 2). These parameters are defined as the time when PCE has been reduced to 80%, 50% and 20% of its initial value and provide a single point parameter to compare lifetimes of the devices. The detailed trend of the full curve has not been fitted, since no clear exponential trend was observed. Although a kink in samples with nonoptimal 5-AVAI weight concentrations was observed, this is still not fully understood but points out that obtaining the optimal concentration (in this case, around 3%) is important not only because it extends the lifetime but also because it qualitatively changes the pattern of degradation.

**Table 2.** Lifetime parameters extracted from degradation trends shown in Figure 4.  $T_X$  is the time at which power conversion efficiency is X% of the initial nominal power conversion efficiency.

Cell	Additive	$T_{80}$	$T_{50}$	$T_{20}$
		Hours	Hours	Hours
A	5-AVAI (1%)	142	328	448
B	5-AVAI (5%)	125	375	544
C	5-AVAI (3%)	550	801	955
D	PABA	0.6	16	48
E	TPA	0.6	1.8	12
F	H3PP	13	21	36

The best lifetime values were found for cell C (3% wt 5-AVAI additive) with  $T_{80} = 550$  h. As can be observed in Figure 4 and Table 2, cells with 5-AVAI showed much better performance than with the other additives. The results for 1% and 5% 5-AVAI additive were

similar in terms of  $T_{80}$ , with cell B (5% 5-AVAI additive) presenting slightly better behavior than the cell with lower 5-AVAI content. The qualitative change of degradation mechanism commented above remains unclear, since it happens both for higher and lower concentrations than the optimal one. A benchmark infiltrated carbon-based mesoporous perovskite solar cell is the one published by Mei et al. with the following parameters for the optimized MAPbI<sub>3</sub> active layer (without AVAI) a  $J_{sc}$  of 13.9 mA/cm<sup>2</sup>, a  $V_{oc}$  of 855 mV, and a FF of 0.61, yielding a PCE of 7.2%; the inclusion of AVAI raised the photocurrent up to 22.8 mA/cm<sup>2</sup>,  $V_{oc}$  was 858 mV, and FF = 0.66, with an improvement of PCE up to 12.84% [44]. The same group pointed out that MAPI cells without AVAI showed  $T_{80}$  around 400 h, and in the most recent results with AVAI stability has grown up to an impressive 9000 h at maximum power point and by cycling day/night operational according to recommendations of IEC61215:2016 [53].

The addition of AVAI in our samples has delivered good performance both in electrical parameters, with the best cell with higher photocurrent but lower open circuit voltage,  $J_{sc} = 21.47$  mA/cm<sup>2</sup>,  $V_{oc} = 810$  mV, FF = 66.53% yielding a good PCE = 11.56% (best cell after light soaking). The trend of degradation showed various stages with different degradation speed. Although there was a nonexponential trend of the  $J_{sc}$  data (Figure 4), which also impacted PCE time evolution, it can be interpreted as multiple stage degradation mechanisms. In the best cell (3% 5-AVAI additive), two regions were distinguished, the first one with a very smooth slope, and after approximately 600 h, a second region with a more pronounced slope. The behavior of the  $J_{sc}$  for cells A and B were more complex with more steeped line shapes. The cells without 5-AVAI showed very pronounced slopes, which could be approximately divided into two regions: an initial very fast decay and a second one with a less pronounced decay. For cell E (TPA additive) the degradation was very fast with a  $T_{80}$  lower than 1h. There was no clear relation between the size of the hysteresis and the lifetime, since longer lifetimes coupled with larger hysteresis (and vice versa) and therefore a correlation between both effects was ruled out in this case.

It has been suggested that the addition of 5-AVAI improves the penetration of the solution during the infiltration of the shell and increases the surface contact, resulting in a lower defect concentration [54]: this effect strongly points that the main effect of 5-AVAI inclusion is avoiding oxygen penetration towards the MAPI, thus extending its lifetime. The role of 5-AVAI is crucial in the formation of superoxide species, which decrease the lifetime of the PSC as result of a combination of different processes, including defect concentration, oxygen diffusion and grain morphology. Devices with 5-AVAI present smaller grains with more surface defects to react with oxygen, due to the higher surface/volume ratio. However, this effect is counterbalanced by an overall lower defect concentration due to the binding of 5-AVAI to iodide vacancies. These vacancies have been reported to be energetically favorable sites for the superoxides formation when the iodide vacancies are occupied by a trapped electron, as they act as trap states in the perovskite bandgap. Additionally, the other effect which lowers the overall superoxide yield is a more compact perovskite layer due to 5-AVAI inclusion, leading to poor oxygen diffusion into the film and thus extending its lifetime [55].

This balance of ultimately beneficial effects of the addition of 5-AVAI is extended to the reduction of oxygen ingress via ETL, either TiO<sub>2</sub> or ZrO<sub>2</sub>, similar to the effect found by Mei et al. [44]. Furthermore, the MAPI crystal structure is modified by 5-AVAI by forming hydrogen bonds between its carboxyl and the iodide ions of MAPI and ammonia groups. Additionally, the presence of the 2D perovskite (HOOC(CH<sub>2</sub>)<sub>4</sub>NH<sub>3</sub>)<sub>2</sub>PbI<sub>4</sub> acting as capping layer on top of a 3D tetragonal phase of MAPI has been shown to strongly enhance stability [45]. The addition of 5-AVAI to the perovskite precursor solution provides additional resistance to degradation. However, the origin of the stability improvement is not yet clear, and it is evident from our results that other molecular additives are not beneficial for the extension of the lifetime.

Additionally, the ZrO<sub>2</sub> layer with optimized thickness of 2 μm provides an isolation that prevents ion migration and a short circuit between the carbon and the TiO<sub>2</sub> layer; it

is not probable that ZrO<sub>2</sub> is providing additional protection to atmospheric degradation agents such as moisture and oxygen [51]. This effect was observed previously, and we consider that the extended lifetime observed in our samples was due to a combination of the effect of the molecular additive and the ZrO<sub>2</sub> layer, but with stronger effect from the additive (improvement in the 5-AVAI case, poor results with the other additives, in both cases containing the same ZrO<sub>2</sub> layer). The carbon top electrode also acts as a barrier against moisture due to the hydrophobic properties of carbon.

## 5. Conclusions

Extended lifetimes have been obtained when 5-aminovaleric acid iodide (5-AVAI) was used as an additive in the active layer of methyl-ammonium lead iodide solar cells. Other molecules were tested as additives, all of them providing poorer results than the 5-AVAI. The best samples with 5-AVAI had PCE higher than 10% and extended lifetime with  $T_{80} = 550$  h. The long lifetime observed in a 1000 h illumination test was the combined effect of engineered interfaces: On the one hand, the molecular additive 5-AVAI was mixed in the active layer, occupying the space between the crystalline grains of the perovskite active layer, but also creating an interlayer at the interface between ETL and carbon layers, preventing ion migration and ingress of moisture and oxygen from the carbon electrode side. Other additives were not effective for this purpose. On the other hand, ZrO<sub>2</sub>, with optimized thickness of 2  $\mu\text{m}$ , prevented ion migration into the TiO<sub>2</sub> layer, but its beneficial effect was lower than the use of the 5-AVAI molecular additive.

**Author Contributions:** R.L.-V. contributed to hypothesis formulation, experimental design, data acquisition and treatment and revision of the manuscript; J.A. and J.P. contributed to experimental design and data acquisition and treatment and manuscript revision and A.U. contributed to hypothesis formulation, experimental design, data treatment and manuscript writing and revision. All authors have read and agreed to the published version of the manuscript.

**Funding:** This research was funded by Ministerio de Ciencia e Innovación-Agencia Estatal de investigación Grant numbers PID2019-104272RB-C55/AEI/10.13039/501100011033 and ENE2016-79282-C5-5-R, and by Fundación Séneca (Región de Murcia) Grant 19882-GERM-15, both including European Commission FEDER funds.

**Institutional Review Board Statement:** Not applicable.

**Informed Consent Statement:** Not applicable.

**Acknowledgments:** Special acknowledgement to Monica Lira-Cantu and Alba Mingorance, Catalan Institute of Nanoscience and Nanotechnology (ICN2) for providing materials and cells and, more importantly, for very useful discussions and access to materials characterization data.

**Conflicts of Interest:** The authors declare no conflict of interest.

## References

1. Lee, M.M.; Teuscher, J.; Miyasaka, T.; Murakami, T.N.; Snaith, H.J. Efficient Hybrid Solar Cells Based on Meso-Superstructured Organometal Halide Perovskites. *Science* **2012**, *338*, 643. [[CrossRef](#)] [[PubMed](#)]
2. Almora, O.; Baran, D.; Bazan, G.C.; Berger, C.; Cabrera, C.I.; Catchpole, K.R.; Erten-Ela, S.; Guo, F.; Hauch, J.; Ho-Baillie, A.W.Y.; et al. Device Performance of Emerging Photovoltaic Materials (Version 1). *Adv. Energy Mater.* **2020**, 2002774. [[CrossRef](#)]
3. Tong, J.; Jiang, Q.; Zhang, F.; Kang, S.B.; Kim, D.H.; Zhu, K. Wide-Bandgap Metal Halide Perovskites for Tandem Solar Cells. *Acc Energy Lett.* **2021**, *6*, 232–248. [[CrossRef](#)]
4. Reese, M.O.; Gevorgyan, S.A.; Jørgensen, M.; Bundgaard, E.; Kurtz, S.R.; Ginley, D.S.; Olson, D.C.; Lloyd, M.T.; Morvillo, P.; Katz, E.A.; et al. Consensus stability testing protocols for organic photovoltaic materials and devices. *Sol. Energy Mater. Sol. Cells* **2011**, *95*, 1253–1267. [[CrossRef](#)]
5. Khenkin, M.V.; Katz, E.A.; Abate, A.; Bardizza, G.; Berry, J.J.; Brabec, C.; Brunetti, F.; Bulović, V.; Burlingame, Q.; Di Carlo, A.; et al. Consensus statement for stability assessment and reporting for perovskite photovoltaics based on ISOS procedures. *Nat. Energy* **2020**, *5*, 35–49. [[CrossRef](#)]
6. Khenkin, M.V.; Anoop, K.M.; Visoly-Fisher, I.; Galagan, Y.; Di Giacomo, F.; Patil, B.R.; Sherafatipour, G.; Turkovic, V.; Rubahn, H.-G.; Madsen, M.; et al. Reconsidering figures of merit for performance and stability of perovskite photovoltaics. *Energy Env. Sci.* **2018**, *11*, 739–743. [[CrossRef](#)]

7. Urbina, A. The balance between efficiency, stability and environmental impacts in perovskite solar cells: A review. *J. Phys. Energy* **2020**, *2*, 022001. [[CrossRef](#)]
8. Calado, P.; Telford, A.M.; Bryant, D.; Li, X.; Nelson, J.; O'Regan, B.C.; Barnes, P.R.F. Evidence for ion migration in hybrid perovskite solar cells with minimal hysteresis. *Nat. Commun.* **2016**, *7*, 13831. [[CrossRef](#)]
9. Liu, D.; Kelly, T.L. Perovskite solar cells with a planar heterojunction structure prepared using room-temperature solution processing techniques. *Nat. Photonics* **2013**, *8*, 133. [[CrossRef](#)]
10. Cao, J.; Wu, B.; Chen, R.; Wu, Y.; Hui, Y.; Mao, B.-W.; Zheng, N. Efficient, Hysteresis-Free, and Stable Perovskite Solar Cells with ZnO as Electron-Transport Layer: Effect of Surface Passivation. *Adv. Mater.* **2018**, *30*, 1705596. [[CrossRef](#)]
11. Im, J.-H.; Jang, I.-H.; Pellet, N.; Grätzel, M.; Park, N.-G. Growth of CH<sub>3</sub>NH<sub>3</sub>PbI<sub>3</sub> cuboids with controlled size for high-efficiency perovskite solar cells. *Nat. Nanotechnol.* **2014**, *9*, 927. [[CrossRef](#)]
12. Matteocci, F.; Cinà, L.; Di Giacomo, F.; Razza, S.; Palma, A.L.; Guidobaldi, A.; D'Epifanio, A.; Licocchia, S.; Brown, T.M.; Reale, A.; et al. High efficiency photovoltaic module based on mesoscopic organometal halide perovskite. *Prog. Photovolt. Res. Appl.* **2016**, *24*, 436. [[CrossRef](#)]
13. Agresti, A.; Taheri, P.S.; Del Rio Castillo, B.; Cinà, A.E.; Bonaccorso, L.F.; Di Carlo, A. Graphene–perovskite solar cells exceed 18% efficiency. A stability study. *Chem. Sus. Chem.* **2016**, *9*, 2609. [[CrossRef](#)] [[PubMed](#)]
14. Malinkiewicz, O.; Yella, A.; Lee, Y.H.; Espallargas, G.M.; Graetzel, M.; Nazeeruddin, M.K.; Bolink, H.J. Perovskite solar cells employing organic charge-transport layers. *Nat. Photonics* **2013**, *8*, 128. [[CrossRef](#)]
15. Jeng, J.-Y.; Chiang, Y.-F.; Lee, M.-H.; Peng, S.-R.; Guo, T.-F.; Chen, P.; Wen, T.-C. CH<sub>3</sub>NH<sub>3</sub>PbI<sub>3</sub> Perovskite/Fullerene Planar-Heterojunction Hybrid Solar Cells. *Adv. Mater.* **2013**, *25*, 3727–3732. [[CrossRef](#)] [[PubMed](#)]
16. Liu, D.; Yang, J.; Kelly, T.L. Compact layer free perovskite solar cells with 13.5% efficiency. *J. Am. Chem. Soc.* **2014**, *136*, 17116. [[CrossRef](#)] [[PubMed](#)]
17. Jeon, Y.-J.; Lee, S.; Kang, R.; Kim, J.-E.; Yeo, J.-S.; Lee, S.-H.; Kim, S.-S.; Yun, J.-M.; Kim, D.-Y. Planar heterojunction perovskite solar cells with superior reproducibility. *Sci. Rep.* **2014**, *4*, 6953. [[CrossRef](#)] [[PubMed](#)]
18. Heo, J.H.; Im, S.H.; Noh, J.H.; Mandal, T.N.; Lim, C.-S.; Chang, J.A.; Lee, Y.H.; Kim, H.; Sarkar, A.; Nazeeruddin, M.K.; et al. Efficient inorganic–organic hybrid heterojunction solar cells containing perovskite compound and polymeric hole conductors. *Nat. Photonics* **2013**, *7*, 486. [[CrossRef](#)]
19. Tian, C.; Castro, E.; Betancourt-Solis, C.E.; Nan, G.; Fernandez-Delgado, Z.; Jankuru, O.S.; Echegoyen, L. Fullerene derivative with a branched alkyl chain exhibits enhanced charge extraction and stability in inverted planar perovskite solar cells. *New J. Chem.* **2018**, *42*, 2896. [[CrossRef](#)]
20. Zhang, H.; Ren, X.; Chen, X.; Mao, J.; Cheng, J.; Zhao, Y.; Liu, Y.; Milic, J.; Yin, W.-J.; Grätzel, M.; et al. Improving the stability and performance of perovskite solar cells via off-the-shelf post-device ligand treatment. *Energy Env. Sci.* **2018**, *11*, 2253–2262. [[CrossRef](#)]
21. Najafi, M.; Di Giacomo, F.; Zhang, D.; Shanmugam, S.; Senes, A.; Verhees, W.; Hadipour, A.; Galagan, Y.; Aernouts, T.; Veenstra, S.; et al. Highly Efficient and Stable Flexible Perovskite Solar Cells with Metal Oxides Nanoparticle Charge Extraction Layers. *Small* **2018**, *14*, 1702775. [[CrossRef](#)]
22. Serrano-Lujan, L.; Espinosa, N.; Larsen-Olsen, T.T.; Abad, J.; Urbina, A.; Krebs, F.C. Tin- and Lead-Based Perovskite Solar Cells under Scrutiny: An Environmental Perspective. *Adv. Energy Mater.* **2015**, *5*, 1501119. [[CrossRef](#)]
23. Chu, L.; Liu, W.; Qin, Z.; Zhang, R.; Hu, R.; Yang, J.; Yang, J.; Li, X. Boosting efficiency of hole conductor-free perovskite solar cells by incorporating p-type NiO nanoparticles into carbon electrodes. *Sol. Energy Mater. Sol. Cells* **2018**, *178*, 164–169. [[CrossRef](#)]
24. Liu, T.; Liu, L.; Hu, M.; Yang, Y.; Zhang, L.; Mei, A.; Han, H. Critical parameters in TiO<sub>2</sub>/ZrO<sub>2</sub>/Carbon-based mesoscopic perovskite solar cell. *J. Power Source* **2015**, *293*, 533–538. [[CrossRef](#)]
25. Bi, D.; Boschloo, G.; Schwarzmüller, S.; Yang, L.; Johansson, E.M.J.; Hagfeldt, A. Efficient and stable CH<sub>3</sub>NH<sub>3</sub>PbI<sub>3</sub>-sensitized ZnO nanorod array solid-state solar cells. *Nanoscale* **2013**, *5*, 11686–11691. [[CrossRef](#)]
26. Kumar, M.H.; Yantara, N.; Dharani, Y.N.; Graetzel, S.; Mhaisalkar, M.S.; Boix, P.P.; Mathews, N. Flexible, low-temperature, solution processed ZnO-based perovskite solid state solar cells. *Chem. Commun.* **2013**, *49*, 11089. [[CrossRef](#)]
27. Son, D.-Y.; Im, J.-H.; Kim, I.J.-H.; Park, N.G. 11% efficient perovskite solar cell based on ZnO nanorods: An effective charge collection system. *J. Phys. Chem.* **2014**, *118*, 16567. [[CrossRef](#)]
28. Carnie, M.J.; Charbonneau, C.; Davies, M.L.; Troughton, J.; Watson, T.M.; Wojciechowski, K.; Snaith, H.; Worsley, D.A. A one-step low temperature processing route for organolead halide perovskite solar cells. *Chem. Commun.* **2013**, *49*, 7893–7895. [[CrossRef](#)]
29. Edri, E.; Kirmayer, S.; Cahen, D.; Hodes, G. High Open-Circuit Voltage Solar Cells Based on Organic–Inorganic Lead Bromide Perovskite. *J. Phys. Chem. Lett.* **2013**, *4*, 897–902. [[CrossRef](#)] [[PubMed](#)]
30. Edri, E.; Kirmayer, S.; Kulbak, M.; Hodes, G.; Cahen, D. Chloride Inclusion and Hole Transport Material Doping to Improve Methyl Ammonium Lead Bromide Perovskite-Based High Open-Circuit Voltage Solar Cells. *J. Phys. Chem. Lett.* **2014**, *5*, 429–433. [[CrossRef](#)] [[PubMed](#)]
31. Seo, S.; Jeong, S.; Bae, C.; Park, N.-G.; Shin, H. Perovskite Solar Cells: Perovskite Solar Cells with Inorganic Electron- and Hole-Transport Layers Exhibiting Long-Term (≈500 h) Stability at 85 °C under Continuous 1 Sun Illumination in Ambient Air (Adv. Mater. 29/2018). *Adv. Mater.* **2018**, *30*, 1870210. [[CrossRef](#)]
32. Liu, C.W.K.; Du, P.; Yi, C.; Meng, T.; Gong, X. Efficient solution-processed bulk heterojunction perovskite hybrid solar cells. *Adv. Energy Mater.* **2015**, *5*, 1402024. [[CrossRef](#)]

33. Christians, J.A.; Schulz, P.; Tinkham, J.S.; Schloemer, T.H.; Harvey, S.P.; Tremolet de Villers, B.J.; Sellinger, A.; Berry, J.J.; Luther, J.M. Tailored interfaces of unencapsulated perovskite solar cells for >1,000 hour operational stability. *Nat. Energy* **2018**, *3*, 68–74. [[CrossRef](#)]
34. Christians, J.A.; Zhang, F.; Bramante, R.C.; Reese, M.O.; Schloemer, T.H.; Sellinger, A.; van Hest, M.F.A.; Zhu, M.K.; Berry, J.J.; Luther, J.M. Stability at scale: Challenges of module interconnects for perovskite photovoltaics. *Acs Energy Lett.* **2018**, *3*, 2502. [[CrossRef](#)]
35. Hao, F.; Stoumpos, C.C.; Cao, D.H.; Chang, R.P.H.; Kanatzidis, M.G. Lead-free solid-state organic–inorganic halide perovskite solar cells. *Nat. Photonics* **2014**, *8*, 489. [[CrossRef](#)]
36. Ma, L.; Hao, F.; Stoumpos, C.C.; Phelan, B.T.; Wasielewski, M.R.; Kanatzidis, M.G. Carrier Diffusion Lengths of over 500 nm in Lead-Free Perovskite  $\text{CH}_3\text{NH}_3\text{SnI}_3$  Films. *J. Am. Chem. Soc.* **2016**, *138*, 14750–14755. [[CrossRef](#)]
37. Hao, F.; Stoumpos, C.C.; Chang, R.P.H.; Kanatzidis, M.G. Anomalous Band Gap Behavior in Mixed Sn and Pb Perovskites Enables Broadening of Absorption Spectrum in Solar Cells. *J. Am. Chem. Soc.* **2014**, *136*, 8094–8099. [[CrossRef](#)]
38. Ogomi, Y.; Morita, A.; Tsukamoto, S.; Saitho, T.; Fujikawa, N.; Shen, Q.; Toyoda, T.; Yoshino, K.; Pandey, S.S.; Ma, T.; et al.  $\text{CH}_3\text{NH}_3\text{Sn}_x\text{Pb}_{(1-x)}\text{I}_3$  Perovskite Solar Cells Covering up to 1060 nm. *J. Phys. Chem. Lett.* **2014**, *5*, 1004–1011. [[CrossRef](#)]
39. Saliba, M.; Orlandi, S.; Matsui, T.; Aghazada, S.; Cavazzini, M.; Correa-Baena, J.-P.; Gao, P.; Scopelliti, R.; Mosconi, E.; Dahmen, K.-H.; et al. A molecularly engineered hole-transporting material for efficient perovskite solar cells. *Nat. Energy* **2016**, *1*, 15017. [[CrossRef](#)]
40. Lira-Cantú, M. Perovskite solar cells: Stability lies at interfaces. *Nat. Energy* **2017**, *2*, 17115. [[CrossRef](#)]
41. Liang, P.-W.; Liao, C.-Y.; Chueh, C.-C.; Zuo, F.; Williams, S.T.; Xin, X.-K.; Lin, J.; Jen, A.K.-Y. Additive Enhanced Crystallization of Solution-Processed Perovskite for Highly Efficient Planar-Heterojunction Solar Cells. *Adv. Mater.* **2014**, *26*, 3748–3754. [[CrossRef](#)]
42. Li, X.; Ibrahim Dar, M.; Yi, C.; Luo, J.; Tschumi, M.; Zakeeruddin, S.M.; Nazeeruddin, M.K.; Han, H.; Grätzel, M. Improved performance and stability of perovskite solar cells by crystal crosslinking with alkylphosphonic acid  $\omega$ -ammonium chlorides. *Nat. Chem.* **2015**, *7*, 703. [[CrossRef](#)]
43. Fu, R.; Zhao, Y.; Li, Q.; Zhou, W.; Yu, D.; Zhao, Q. Enhanced long-term stability of perovskite solar cells by 3-hydroxypyridine dipping. *Chem. Commun.* **2017**, *53*, 1829–1831. [[CrossRef](#)]
44. Mei, A.; Li, X.; Liu, L.; Ku, Z.; Liu, T.; Rong, Y.; Xu, M.; Hu, M.; Chen, J.; Yang, Y.; et al. A hole-conductor-free, fully printable mesoscopic perovskite solar cell with high stability. *Science* **2014**, *345*, 295. [[CrossRef](#)]
45. Grancini, G.; Roldán-Carmona, C.; Zimmermann, I.; Mosconi, E.; Lee, X.; Martineau, D.; Narbey, S.; Oswald, F.; De Angelis, F.; Grätzel, M.; et al. One-Year stable perovskite solar cells by 2D/3D interface engineering. *Nat. Commun.* **2017**, *8*, 15684. [[CrossRef](#)]
46. Santhosh, N.; Sitaaraman, S.R.; Pounraj, P.; Govindaraj, R.; Pandian, M.S.; Ramasamy, P. Fabrication of hole-transport-free perovskite solar cells using 5-ammonium valeric acid iodide as additive and carbon as counter electrode. *Mater. Lett.* **2019**, *236*, 706–709. [[CrossRef](#)]
47. Hou, X.; Huang, S.; Ou-Yang, W.; Pan, L.; Sun, Z.; Chen, X. Constructing Efficient and Stable Perovskite Solar Cells via Interconnecting Perovskite Grains. *Acs Appl. Mater. Interfaces* **2017**, *9*, 35200–35208. [[CrossRef](#)]
48. Zhang, C.; Luo, Q.; Deng, X.; Zheng, J.; Ou-Yang, W.; Chen, X.; Huang, S. Enhanced efficiency and stability of carbon based perovskite solar cells using terephthalic acid additive. *Electrochim. Acta* **2017**, *258*, 1262–1272. [[CrossRef](#)]
49. Zou, Y.; Liang, Y.; Mu, C.; Zhang, J.-P. Enhancement of Open-Circuit Voltage of Perovskite Solar Cells by Interfacial Modification with p-Aminobenzoic Acid. *Adv. Mater. Interfaces* **2020**, *7*, 1901584. [[CrossRef](#)]
50. Li, B.; Chen, Y.; Liang, Z.; Gao, D.; Huang, W. Interfacial engineering by using self-assembled monolayer in mesoporous perovskite solar cell. *RSC Adv.* **2015**, *5*, 94290–94295. [[CrossRef](#)]
51. Mingorance, A.; Xie, H.; Kim, H.-S.; Wang, Z.; Balsells, M.; Morales-Melgares, A.; Domingo, N.; Kazuteru, N.; Tress, W.; Fraxedas, J.; et al. Interfacial Engineering of Metal Oxides for Highly Stable Halide Perovskite Solar Cells. *Adv. Mater. Interfaces* **2018**, *5*, 1800367. [[CrossRef](#)]
52. Meng, L.; You, J.; Guo, T.-F.; Yang, Y. Recent Advances in the Inverted Planar Structure of Perovskite Solar Cells. *Acc. Chem. Res.* **2016**, *49*, 155–165. [[CrossRef](#)] [[PubMed](#)]
53. Mei, A.; Sheng, Y.; Ming, Y.; Hu, Y.; Rong, Y.; Zhang, W.; Luo, S.; Na, G.; Tian, C.; Hou, X.; et al. Stabilizing Perovskite Solar Cells to IEC61215:2016 Standards with over 9,000-h Operational Tracking. *Joule* **2020**, *4*, 2646–2660. [[CrossRef](#)]
54. Lin, C.-T.; De Rossi, F.; Kim, J.; Baker, J.; Ngiam, J.; Xu, B.; Pont, S.; Aristidou, N.; Haque, S.A.; Watson, T.; et al. Evidence for surface defect passivation as the origin of the remarkable photostability of unencapsulated perovskite solar cells employing aminovaleric acid as a processing additive. *J. Mater. Chem. A* **2019**, *7*, 3006–3011. [[CrossRef](#)]
55. Péan, E.V.; De Castro, C.S.; Dimitrov, S.; De Rossi, F.; Meroni, S.; Baker, J.; Watson, T.; Davies, M.L. Investigating the Superoxide Formation and Stability in Mesoporous Carbon Perovskite Solar Cells with an Aminovaleric Acid Additive. *Adv. Funct. Mater.* **2020**, *30*, 1909839. [[CrossRef](#)]